Terahertz-field-induced second optical harmonic generation from Si(111) surface

S. B. Bodrov,[1,2,*] Yu. A. Sergeev,[1,2] A. I. Korytin,[1] and A. N. Stepanov[1]
[1]*Institute of Applied Physics, Russian Academy of Sciences, Nizhny Novgorod 603950, Russia*
[2]*University of Nizhny Novgorod, Nizhny Novgorod 603022, Russia*

(Received 28 October 2021; accepted 8 December 2021; published 18 January 2022)

We study, both experimentally and theoretically, the second-harmonic (SH) generation (SHG) of optical radiation assisted by intense terahertz electromagnetic pulses from the surface of high-resistivity Si(111). The study was performed within the framework of the analysis of the superposition of different SH sources, including the surface-dipole, bulk-quadruple, and electric-field-induced (EFI) bulk-dipole (arising from internal built-in and external terahertz fields) contributions. Azimuthal rotation anisotropy of SHG for an arbitrary mutual polarization of the terahertz, fundamental, and SH optical fields was calculated and experimentally verified. The strongest impact of the terahertz field on SHG was observed in the case where the polarizations of the terahertz and SH fields coincide. In these polarization configurations, the terahertz field added mainly an isotropic term to the SH azimuthal dependences. It has been demonstrated that the application of the terahertz field can be helpful for distinguishing the SHG mechanism. For the sample under study, the contribution to the SH energy from the built-in field-induced source was found to be >4 times greater than the contribution from the surface and quadrupole nonlinear sources. The dominance of the EFISHG allowed us to find the ratio between the components of a silicon third-order nonlinear tensor $\chi^{(3)}(2\omega;\omega,\omega,0)$: $\chi_{1122}=\chi_{1212}\approx 0.51\chi_{1111}$ and $\chi_{1212}\approx\chi_{1221}$ for the fundamental optical wavelength 790 nm.

DOI: 10.1103/PhysRevB.105.035306

I. INTRODUCTION

Silicon is one of the most important materials in the semiconductor industry, primarily in microelectronics. In many silicon applications, electrophysical processes occurring on the surface of silicon and its interface with other materials play an important role. One of the effective methods for surface diagnostics is the second-harmonic (SH) generation (SHG) of optical radiation [1–5]. Indeed, silicon belongs to the media with an inversion center, where SHG is forbidden in the bulk (in the electric-dipole approximation), but the surface breaks the symmetry, which permits nonlinear frequency doubling. In this regard, SHG is extremely sensitive to the condition of the surface.

Due to the rather weak nonlinear conversion efficiency from the surface, high intensities of fundamental optical radiation are required for sensing the generated SH. To prevent thermal damage, laser pulses of femtosecond (or picosecond) duration are commonly used. Two main SH measuring techniques for sample characterization are generally employed. The first is a rotational anisotropy SHG technique, in which the SH energy (signal) is measured as a function of the azimuthal angle of rotation relative to the normal of the surface [3,4,6,7]. This technique permits one to characterize the symmetry of the sample surface, as well as the surface reconstruction [8,9], interfacial preparation (thermal or ambient oxidation, etching, etc.) [10–14], microroughness [12,15], step-edge structure [16–20], strain [21,22], etc. The second is a SH spectroscopy technique, in which the SH signal is measured as a function of the fundamental harmonic frequency [16,23–26]. Such a technique helps one study the resonant properties of the SH excitation and provides information about the silicon band structure and its modification near the surface [3,13,26–29]. Phase-sensitive measurements can additionally be used in both techniques for more complete information about the sample [27,30,31].

Three main SHG mechanisms were established in previous studies [1,3]. The first is associated with the formation of the dipole nonlinear polarization (NP) in the symmetry-breaking region with a thickness of several atomic layers due to the presence of broken bonds of silicon atoms. The second mechanism is of quadrupole nature and is due to the spatial field gradient of the fundamental harmonic in the bulk of silicon. The third mechanism is determined by the electric-field-induced (EFI) SHG (EFISHG) effect [32] due to the existence of a built-in electric field in a space charge region near the silicon surface [33,34]. The first SHG mechanism can be considered as purely surface, whereas the last two mechanisms have a bulk localization. The ratio of the mechanisms to the total SH signal significantly depends on the Si doping level, the preliminary preparation of the sample surface, its quality, etc. [13,18,20,26,35–37]. Finding the dominant contribution is not a trivial task [1,3,31,38].

Characterization of the built-in field and the space charge region is essential for the operation of many Si-based microelectronic devices [e.g., metal-oxide-semiconductor (MOS) transistors and capacitors]. Most commonly, capacitance-voltage measurements [39] are used for this purpose. However, such measurements require the fabrication of an

*sergey.bodrov@ipfran.ru

 ©2022 American Physical Society

electrode structure which can affect the interface properties, lead to additional transport and trapping of mobile carriers across the silicon interface [40], and cause a breakdown of thin dielectric films (<10 nm) used in modern MOS structures [41]. In contrast, the SHG offers additional advantages for nondestructive, contactless diagnostics [4,42]. For this purpose, a time-dependent SHG (TD-SHG) measurement [42–47], where the SH signal is traced as a function of the optical exposure time, can be used. The TD-SHG effect is related to multiphoton ionization, injection, transport, and trapping of the optically induced charge carriers in the interface and in the silicon oxide (or in another silicon-covering dielectric). The time behavior of the SH signal can reveal the silicon dopant type [45], applied bias [46], as well as the oxide thickness [44], roughness, thermal processing steps, and the presence of metal contamination [42]. However, TD-SHG gives only a relative measurement, which requires calibration.

A more relevant approach for the built-in field characterization is based on using an external electric field applied to the sample [31,48,49]. An experimental demonstration of this so-called EFISHG technique in silicon using an electrolyte was reported by Lee *et al.* [50]. For MOS structures, intense research started in the early 1990s. In a pioneering work of the group led by Aktsipetrov [51], a significant effect of an external DC electric field on the SH signal at the Si-SiO_2 interface was shown for the n-type Si(111)/SiO_2 structure with an InGa top electrode. In the subsequent examination of various silicon samples, more detailed theoretical and experimental studies have been carried out, and a deeper understanding of the physical processes accompanying the EFISHG effect has been achieved. An electrophysical model has been developed considering the self-consistent spatial distribution of the built-in electric field and space charge in the near-surface region [49,52,53]. In Ref. [54], carrier-induced screening of the electric field at the Si(001)-SiO_2 interface was observed and discussed. Contributions to the resulting SH signal from surface (interphase) and EFI bulk SH sources were debated [30,48,49,53,55–57]. It should be noted that the EFISHG technique encounters some difficulties in explaining the experimental results due to the influence of metal contacts on SHG [37] and the effect of the applied voltage on the space charge [49,52,58] with an accompanying possible distortion of the electric field near the metal contacts. Also, the metallization (or immersion of the sample in an electrolyte) can lead to a modification of the surface under study [48].

Instead of the DC electric field, a freely propagating low-frequency electromagnetic field can be applied to the sample. For example, the field of short terahertz pulses coherently generated by optical-to-terahertz conversion of femtosecond laser radiation can be employed. In this so-called terahertz-field-induced (TFI) SHG (TFISHG) technique, the duration of a femtosecond optical pulse of the fundamental harmonic is typically several times shorter than the period of the terahertz oscillation, which permits one to consider the terahertz field as quasistatic. In contrast to a DC field, the use of terahertz pulses does not require the manufacture of conductive contacts, allows free control of the field polarization, and gives an opportunity to study the low-frequency dispersion of the SH response by measuring the time delay between terahertz and optical pulses [59,60]. Also, the picosecond duration of the terahertz pulse makes it possible to apply a field higher than the DC breakdown field. For example, in Ref. [60], p-doped silicon was explored by TFISHG using superstrong (up to 20 MV/cm) terahertz fields. The effect of the ponderomotive force of such extreme terahertz pulses and the modulation of the TFI impact ionization rate at the optical frequency on the SH signal was demonstrated.

In this paper, we demonstrate the possibility of effective use of TFISHG to characterize crystalline silicon. By using Ti:sapphire femtosecond laser pulses in combination with coherent terahertz pulses having a peak electric field of up to 250 kV/cm, we studied the optical SHG from high-resistivity Si(111) with native oxide. Anisotropy of SHG was calculated and measured for different mutual orientations of the terahertz, fundamental, and SH optical electric fields. The SH field phase between surface/bulk-quadruple and EFI bulk contributions was extracted by applying a terahertz field. Comparison of experimental data with the theory made it possible to reveal the relative role of various mechanisms of SHG, to measure the ratio between the components of a third-order nonlinear tensor, and to estimate the magnitude of the built-in field.

This paper is organized as follows. In Sec. II, we extend the theory of the EFISHG rotation anisotropy for Si(111), considering the arbitrary polarization of an external (terahertz) electric field, and discuss the electrodynamics of SHG within the framework of the superposition of surface-dipole, bulk-quadruple, and EFI SH sources. In Sec. III, we present the experimental results and, comparing them with the theory, characterize the sample properties, such as the dominant SHG mechanism, the third-order nonlinear tensor, and the built-in electric field.

II. THEORY

The theory of the surface SHG, including the EFISHG effect, has been developed in several publications (see review articles [1,3]). However, in previous studies, the rotation anisotropy of SHG was considered for a single orientation of the electric field (internal or external) perpendicular to the surface. Below, we derive general expressions of EFISHG anisotropy for an arbitrary direction of the external electric field (terahertz field in this case) for a (111)-oriented Si surface and discuss the phase relation of SH fields from surface and bulk nonlinear sources contributing to the total generated SH energy.

Figure 1 shows the geometry of the problem. Si(111) is illuminated by optical and terahertz pulses with arbitrary polarization. Incidence angles of the optical and terahertz pulses in Fig. 1 are shown equal (this corresponds to our experimental condition where the angles were ∼45°); however, these angles may be arbitrary (as well as differ from each other) in the further theoretical consideration. We assume that the duration of the optical pulse is much shorter than the period of the terahertz wave. In this case, the terahertz electric field $\mathbf{E}_0^T$ can be considered as quasistatic with respect to the optical pulse. Inside silicon, near the surface, we consider the existence of a built-in electric field $\mathbf{E}^B = \hat{\mathbf{z}}E^B(z)$, where the z axis is normal to the surface. The strength of the field is determined by trapped electrons at the silicon interface

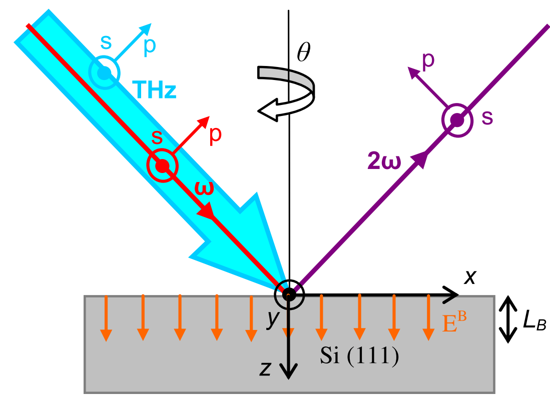

FIG. 1. Geometry of the problem for calculation of the terahertz-field-induced second-harmonic (SH) nonlinear polarization.

and/or in an insulator (silicon oxide) film typically covering the silicon surface. The field localization length L^B in silicon is governed by both the silicon doping level and the surface potential [33,34,61]. It is assumed that the sample can rotate around an axis perpendicular to the surface at an azimuthal angle θ (the positive direction of rotation is chosen clockwise when the sample is viewed from above). The crystallographic axes of the crystal are directed so that, at $\theta = 0$, the x, y, and z axes of the laboratory coordinate system coincide with the crystallographic directions $[2\bar{1}\bar{1}]$, $[01\bar{1}]$, and $[111]$, respectively.

SH NP $\mathbf{P}_{\mathrm{SH}}$ induced near the surface can be expressed as the superposition of four terms:

$$\mathbf{P}_{\mathrm{SH}} = \mathbf{P}^S + \mathbf{P}^Q + \mathbf{P}^B + \mathbf{P}^T. \tag{1}$$

Here, $\mathbf{P}^S$ is the dipole NP arising near the surface due to the broken symmetry of the crystal lattice on the scale of several atomic layers. The NP can be expressed by a $\hat{\chi}^{(2)}$ surface tensor. Here, $\mathbf{P}^Q$ is the quadrupole bulk NP, which appears due to the spatial dispersion and is expressed by a quadrupole tensor $\hat{\chi}^{(3)Q}$. Also, $\mathbf{P}^B$ and $\mathbf{P}^T$ are the EFI NPs related to the bulk cubic nonlinearity $\hat{\chi}^{(3)}$ in the presence of built-in $\mathbf{E}^B$ and external $\mathbf{E}_0^T$ electric fields, respectively. Note that, in atmospheric air, silicon is covered with a native oxide layer 1–2 nm thick [13,14,62]. Therefore, the same NPs can be induced in this layer. Nevertheless, due to the small layer thickness, these additional NPs can be included in $\mathbf{P}^S$, which can then be considered as an interfacial Si-$\mathrm{SiO_2}$ NP.

Expressions for P_j^S, P_j^Q, and P_j^B ($j = x, y, z$) as functions of the azimuthal angle θ in the laboratory coordinate system can be found in Refs. [1,7]. To calculate the angular anisotropy of $P_j^T(\theta)$ (induced by arbitrarily oriented $\mathbf{E}_0^T$), we use the approach described in Ref. [1]. First, we transform the optical and terahertz electric fields from the laboratory to the crystallographic coordinate system using successively the rotation matrix:

$$A_{ij} = \begin{bmatrix} \cos(\theta) & \sin(\theta) & 0 \\ -\sin(\theta) & \cos(\theta) & 0 \\ 0 & 0 & 1 \end{bmatrix}, \tag{2}$$

and the transformation matrix:

$$B_{ij} = \begin{bmatrix} \frac{2}{\sqrt{6}} & 0 & \frac{1}{\sqrt{3}} \\ -\frac{1}{\sqrt{6}} & \frac{1}{\sqrt{2}} & \frac{1}{\sqrt{3}} \\ -\frac{1}{\sqrt{6}} & -\frac{1}{\sqrt{2}} & \frac{1}{\sqrt{3}} \end{bmatrix}, \tag{3}$$

defined by the orientation of the crystallographic axes relative to the surface. Then in the crystallographic coordinate system, we calculate the EFI NP by using a nonlinear tensor $\hat{\chi}^{(3)}$ [1]:

$$\begin{aligned} &\chi^{(3)}_{1111} = \chi^{(3)}_{2222} = \chi^{(3)}_{3333} = \chi_1, \\ &\chi^{(3)}_{1122} = \chi^{(3)}_{2211} = \chi^{(3)}_{1133} = \chi^{(3)}_{3311} = \chi^{(3)}_{3322} = \chi^{(3)}_{2233} = \chi_2, \\ &\chi^{(3)}_{1212} = \chi^{(3)}_{2121} = \chi^{(3)}_{1313} = \chi^{(3)}_{3131} = \chi^{(3)}_{3232} = \chi^{(3)}_{2323} = \chi_2, \\ &\chi^{(3)}_{1221} = \chi^{(3)}_{2112} = \chi^{(3)}_{1331} = \chi^{(3)}_{3113} = \chi^{(3)}_{3223} = \chi^{(3)}_{2332} = \chi_3. \end{aligned} \tag{4}$$

After that, the obtained expression for the NP was transformed back to the laboratory coordinate system, using matrixes inverse of Eqs. (2) and (3). The result of the calculation of $P_j^T(\theta)$ is given in Table I. Also, Table I contains the surface and the built-in field-induced NPs [$P_j^S(\theta)$ and $P_j^B(\theta)$, respectively] reproduced from Ref. [1] ($P_j^Q(\theta)$ is not shown in Table I but can be found in Ref. [1]). In expressions for the NPs, the fields E_j and E_j^T are the j components ($j = x, y, z$) of the optical and terahertz fields inside silicon (E_j^T is related to the incident terahertz field E_{0j}^T by Fresnel formulas). The constant $\chi_0 = \sqrt{2}(\chi_1 - 2\chi_2 - \chi_3)/6$ is some combination of $\hat{\chi}^{(3)}$ tensor components, which characterize the bulk nonlinear anisotropy (note that, for an isotropic medium, $\chi_0 = 0$) [1]. The notation of field polarizations is written as RR or RRR (R = S, P), where the first and last letters denote the polarizations of the fundamental and SHs, respectively, and the intermediate letter (if any) denotes the terahertz field polarization.

The azimuthal dependences of all NPs $\mathbf{P}^k(\theta)$, $k = S$, B, T, Q, include both isotropic (independent of the angle θ) and threefold anisotropic [proportional to $\sin(3\theta)$ or $\cos(3\theta)$] terms. Note that, without terahertz radiation, the NPs $\mathbf{P}^k(\theta)$, $k = S$, B, Q, and their superposition $\mathbf{P}^0_{\mathrm{SH}}(\theta) = \mathbf{P}^S(\theta) + \mathbf{P}^Q(\theta) + \mathbf{P}^B(\theta)$ have an identical angular anisotropy. The application of a terahertz field leads to a change in the NP azimuthal dependence for some polarization configuration. For example, in the SS case characterized by fully anisotropic $\mathbf{P}^0_{\mathrm{SH}}(\theta) \sim \sin(3\theta)$, the application of an s-polarized terahertz field (the SSS case) adds an isotropic term, while the p-polarized terahertz field (the SPS case) adds an anisotropic term and does not modify the dependence. Analyzing all cases of polarization configuration, two general conclusions can be drawn from Table I. First, the isotropic term in $\mathbf{P}^T(\theta)$ rises only when the polarizations of the terahertz and SH fields are the same, i.e., in the SSS, PSS, SPP, and PPP cases. Second, the anisotropic terms in $\mathbf{P}^T(\theta)$ are always proportional to the anisotropy constant χ_0.

We now focus on the electrodynamics of SHG, or rather on the result of the interference of the SH fields induced by $\mathbf{P}^0_{\mathrm{SH}}$ and $\mathbf{P}^T$. The SH electric field generated by the total NP defined by Eq. (1) can be represented as the superposition of

TABLE I. Expressions for the Cartesian components of the SH NP for various sources in the laboratory coordinate system.

SH NP	Surface contribution[a,b]	Built-in field contribution[a]	Terahertz contribution: s polarization	Terahertz contribution: p polarization
		SS	SSS	SPS
P_y^{SH}	$-E_y^2\chi_{111}^{(2)}\sin(3\theta)$	$-E_y^2E^B\chi_0\sin(3\theta)$	$E_y^2E_y^T(\chi_1-3\chi_0/\sqrt{2})$	$-E_y^2E_z^T\chi_0\sin 3\theta$
		PS	PSS	PPS
P_y^{SH}	$E_x^2\chi_{111}^{(2)}\sin(3\theta)$	$E_x^2E^B\chi_0\sin(3\theta)$	$E_y^T\begin{bmatrix}E_x^2(\chi_0/\sqrt{2}+\chi_3)\\+E_z^2(\sqrt{2}\chi_0+\chi_3)\\-2E_xE_z\chi_0\cos(3\theta)\end{bmatrix}$	$(2E_xE_zE_x^T+E_x^2E_z^T)\chi_0\sin 3\theta$
		SP	SSP	SPP
P_x^{SH}	$-\chi_{111}^{(2)}E_y^2\cos(3\theta)$	$-E_y^2E^B\chi_0\cos(3\theta)$	0	$E_y^2\begin{bmatrix}E_x^T(\chi_0/\sqrt{2}+\chi_3)\\-E_z^T\chi_0\cos(3\theta)\end{bmatrix}$
P_z^{SH}	$\chi_{311}^{(2)}E_y^2$	$E_y^2E^B(\sqrt{2}\chi_0+\chi_3)$	$-E_y^2E_y^T\chi_0\sin 3\theta$	$E_y^2\begin{bmatrix}E_z^T(\sqrt{2}\chi_0+\chi_3)\\-E_x^T\chi_0\cos(3\theta)\end{bmatrix}$
		PP	PSP	PPP
P_x^{SH}	$2\chi_{113}^{(2)}E_xE_z+\chi_{111}^{(2)}E_x^2\cos(3\theta)$	$2E_xE_zE^B(\sqrt{2}\chi_0+\chi_2)$ $+E_x^2E^B\chi_0\cos(3\theta)$	$2E_y^TE_xE_z\chi_0\sin(3\theta)$	[c]
P_z^{SH}	$\chi_{311}^{(2)}E_x^2+\chi_{333}^{(2)}E_z^2$	$E_z^2E^B(\chi_1-2\sqrt{2}\chi_0)$ $+E_x^2E^B(\sqrt{2}\chi_0+\chi_3)$	$E_y^TE_x^2\chi_0\sin(3\theta)$	[d]

[a]Reference [1].
[b]The axes of the coordinate system (100), (010), and (001), in which the surface tensor is written, coincide with the x, y, and z axes at $\theta=0$, respectively.
[c]$E_x^2E_x^T(\chi_1-\frac{3}{\sqrt{2}}\chi_0)+E_z^2E_x^T(\sqrt{2}\chi_0+\chi_3)+2E_xE_zE_z^T(\sqrt{2}\chi_0+\chi_2)+(E_x^2E_z^T+2E_xE_zE_x^T)\chi_0\cos(3\theta)$.
[d]$E_z^2E_z^T(\chi_1-2\sqrt{2}\chi_0)+E_x^2E_z^T(\sqrt{2}\chi_0+\chi_3)+2E_xE_zE_x^T(\sqrt{2}\chi_0+\chi_2)+E_x^2E_x\chi_0\cos 3\theta$.

SH fields $\mathbf{E}_{SH}^k$ from each $\mathbf{P}^k$ ($k=S,Q,B,T$):

$$\mathbf{E}_{SH}=\mathbf{E}_{SH}^S+\mathbf{E}_{SH}^Q+\mathbf{E}_{SH}^B+\mathbf{E}_{SH}^T. \quad (5)$$

Here, $\mathbf{E}_{SH}^k$ can be calculated by the Green's function method with allowance for boundary conditions [1,7,30,63,64]:

$$\mathbf{E}_{SH}^k=\int_0^\infty \mathbf{G}(z-z')\mathbf{P}^k(z')dz', \quad (6)$$

where $\mathbf{G}$ is the Green's function [64]. The integration result of Eq. (6) significantly depends on the space localization of $\mathbf{P}^k(z)$. The surface NP can be written in terms of the delta function $P_j^S(z)\sim\delta(z)$. For bulk SH sources, NPs can be written via the spatial factor [1] $P_j^k(z)\sim\exp(-i2\kappa_\omega z-z/L^k)$ ($k=Q,B,T$), where κ_ω is the wave number of the fundamental field in silicon, $L^Q\to\infty$, and L^T is the space (localization) length of the terahertz field.

The exact expressions for $\mathbf{E}_{SH}^S$, $\mathbf{E}_{SH}^Q$, and $\mathbf{E}_{SH}^B$ calculated by Eq. (6) are given in Refs. [1,61,64]. The expression for $\mathbf{E}_{SH}^T$ can be obtained from $\mathbf{E}_{SH}^B$ by replacing the length L^B with L^T. We will not present these exact expressions here but restrict ourselves to analyzing the phases φ^k ($k=S$, Q, B, T) of the generated SH fields $\mathbf{E}_{SH}^k\sim\exp(i2\omega t+i\varphi^k)$ (ω is the cyclic frequency of the fundamental harmonic) since these phases affect the field interference and, as a consequence, the resulting SH rotation anisotropy. The phases φ^k are affected both by the resonance properties of the nonlinear response of silicon (mathematically, resonances are the cause of the complex value of the corresponding nonlinear tensor) and by the electrodynamics of the SH field formation [mathematically, it is expressed by the convolution in Eq. (6)]. Next, we focus on the case where the frequencies of the first and SHs are far from silicon resonances, which corresponds to our experimental conditions, where the fundamental field at the central wavelength $\lambda_\omega=790$ nm was used (see also the discussion in Sec. III). This assumption allows us to consider the surface and EFI NPs as real and the quadrupole NP as imaginary [$P_j^Q=\chi_{jmql}^{(3)Q}E_m\nabla_qE_l\approx i\chi_{jmql}^{(3)Q}E_m(\kappa_\omega)_qE_l$]. In this case, the phases φ^k will be determined by the ratio between L^k and the SH space length $L_{SH}\approx 1/|k_{2\omega}|$, where $k_{2\omega}$ is the SH wave number in silicon. When $L_{SH}\ll L^k$, Eq. (6) gives $\varphi^k\sim 0$ (or π) for real NP and $\varphi^k\sim\pm\pi/2$ for imaginary NP, and when $L_{SH}\gg L^k$, vice versa, $\varphi^k\sim 0$ (or π) for imaginary NP and $\varphi^k\sim\pm\pi/2$ for real NP.

Following the above analysis, for the surface and quadrupole SH source in the nonresonance case, we have $\varphi^S\approx\varphi^Q\approx 90^\circ$. More accurate calculation with allowance for complex Si refractive indexes gives a slight phase change; for example, for $\lambda_\omega=790$ nm, we have $\varphi^S=95^\circ$. The phase φ^B can vary significantly for different silicon samples due to the abovementioned strong dependence of the built-in field localization length L^B on both the Si doping and the surface potential. Indeed, L^B can range from several nanometers (for Si with a carrier concentration $n_c>10^{18}$ cm^{-3}) to several micrometers (for intrinsic Si with $n_c\sim 10^{10}$ cm^{-3} and a small, <0.1 V, surface potential) [61,65]. Figure 2 shows φ^B as a function of L^B calculated for $\lambda_\omega=790$ nm (the calculation is based on the equation for $\mathbf{E}_{SH}^B$ given in Refs. [1,61] with allowance for the complex value of the silicon optical refractive indices). It can be seen that increasing L^B from 0 to $L_{SH}\sim 50$ nm rapidly changes φ^B from 95° to 165°; for

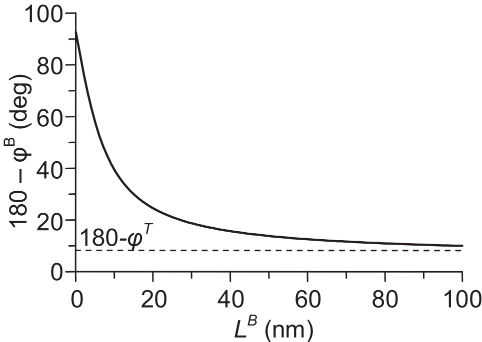

FIG. 2. Phase φ^B as a function of the nonlinear polarization (NP) localization length L^B calculated for a fundamental wavelength of 790 nm.

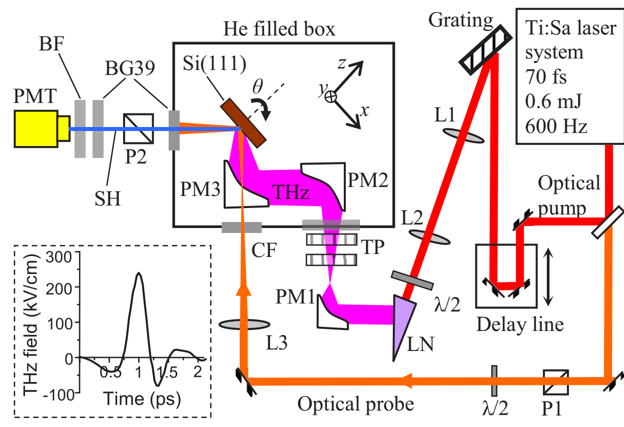

FIG. 3. Experimental setup.

$L^B > 50$ nm, φ^B tends to a constant level of $\sim 170^\circ$. The phase φ^T can be taken close to 180° in a wide range of the Si doping level. Indeed, even for high $n_c \sim 10^{18}$–10^{19} cm^{-3}, the penetration length of the terahertz field at a frequency of $\sim$1 THz is $\sim$1 μm, which is at least several times more than $L_{\rm SH}$ for fundamental frequency above the silicon bandgap. In high-resistivity (>1 kΩ/cm) Si, the terahertz field does not significantly attenuate and can be considered as uniform on the $L_{\rm SH}$ scale, which gives $\varphi^T \approx 170^\circ$ for $\lambda_\omega = 790$ nm (Fig. 2).

Based on the above discussion, it can be concluded that, for most of the Si samples explored far from the optical resonances, the TFI SH field $\mathbf{E}^T_{\rm SH}$ does not interfere with the SH fields generated by surface and quadrupole sources, $\mathbf{E}^S_{\rm SH}$ and $\mathbf{E}^Q_{\rm SH}$, respectively. At the same time, $\mathbf{E}^T_{\rm SH}$ can partially interfere with the SH field $\mathbf{E}^B_{\rm SH}$ induced by the built-in field. Then neglecting the imaginary part of the silicon refractive indices, the rotation anisotropy of the generated SH energy (signal) for an arbitrary polarization configuration can be written in the following form:

$$W_{\rm RRR}(\theta) = \left| \left\{ \left[F^S_{\rm RR}(\theta) + F^Q_{\rm RR}(\theta)\right] \exp\left(\frac{i\pi}{2}\right) + F^B_{\rm RR}(\theta)\exp(i\varphi^B) \right\} + F^T_{\rm RRR}(\theta)\exp(i\varphi^T) \right|^2, \tag{7}$$

where the real functions $F^k_{\rm RR}(\theta)$ ($k = S, Q, B$) and $F^T_{\rm RRR}(\theta) = A^T_{\rm RRR}(\theta)E^T_0$ [functions $A^T_{\rm RRR}(\theta)$ are also assumed real] consider both the electrodynamics of the SH field emission [governed by Eq. (6)] and the azimuthal dependences of the NPs for the corresponding polarization configuration (RR or RRR, R = S, P). Note that the functions $F^k_{\rm RR}(\theta)$ have the same angular dependence. For a further theoretical and experimental comparison, it is convenient to discriminate the anisotropic and anisotropic terms in Eq. (7). Considering the complexity of the refractive indices and components of the nonlinear tensors [$\hat{\chi}^{(2)}$, $\hat{\chi}^{(3)}$, and $\hat{\chi}^{(3)Q}$], Eq. (7) can also be written in a general form:

$$W_{\rm RRR}(\theta) = \left|\left[A^{\rm i}_{\rm RR}\exp\left(i\varphi^{\rm i}_{\rm RR}\right) + A^{\rm a}_{\rm RR}(\theta)\exp\left(i\varphi^{\rm a}_{\rm RR}\right)\right] + A^T_{\rm RRR}(\theta)E^T_0\right|^2, \tag{8}$$

where $A^{\rm i,a}_{\rm RR}$ and $\varphi^{\rm i,a}_{\rm RR}$ are the amplitudes and relative phenomenological phases of the isotropic (i) and anisotropic (a) components of the SH field generated without the external terahertz field.

III. EXPERIMENTAL RESULTS AND DISCUSSION

The experimental setup used to study SHG from the sample surface in the presence of strong terahertz fields is shown in Fig. 3. Radiation of a Ti:sapphire laser system (0.6 mJ, 795 nm, 70 fs, and 600 Hz) was split into two beams. The main part of the optical energy was used to generate terahertz pulses by the tilted-pulse-front technique in a $LiNbO_3$ crystal (the tilted intensity front was created by a 1800 mm^{-1} grating and imaged in the crystal by lenses L1 and L2 with focal lengths of 25 and 15 cm, respectively) [66,67]. The terahertz radiation generated from the crystal had a vertical (s) polarization (normal to the drawing plate). Terahertz pulses were sharply focused on the sample using a system of off-axis parabolic mirrors PM1–PM3. Two terahertz thin film polarizers (TPs) were used to attenuate the terahertz field as well as to change its polarization. Note that the s- to p-polarization conversion reduces the amplitude of the terahertz field by about two times but permits one to control the direction of the p-polarized field (the terahertz electric fields with positive and negative projection on the x axis are denoted $\rm P_+$ and $\rm P_-$, respectively).

The magnitude of the terahertz field was measured using a classical electro-optic sampling technique (not shown in the figure) by detection of the field-induced depolarization of the probe laser radiation in a 200-μm-thick GaP crystal. The maximum value of the terahertz field (with s polarization) at the focus of the parabolic mirror (PM3) reached $\sim$250 kV/cm (see the inset in Fig. 3). To determine the direction of the terahertz field, the 200 μm GaP crystal was replaced by a 3-mm-thick (110) ZnTe crystal sandwiched between DC-voltage-biased metal plates. Comparison of the optical depolarization induced by terahertz and DC fields allowed us to specify the direction of the terahertz field at its maximum as coinciding with the y axis (see Fig. 3).

Another part of the optical radiation (probe beam) was used to generate the second optical harmonic from the sample. The probe laser pulses were focused by lens L3 on the sample at an

angle of 45° collinear with the terahertz pulses to a spot size of ∼150 μm, which is less than the size of the terahertz beam, being ∼500 μm (the pulse alignment occurred through a hole in the off-axis parabolic mirror PM3). The maximum intensity of optical radiation on the sample was ∼ 10 GW/cm^2. The delay line was set to make the optical pulse coincide with the maximum value of the terahertz field. The polarization of the probe pulse was rotated by a λ/2 plate and filtered using a P1 polarizing plate (Thorlabs WP25L-UB).

In the experiment, *n*-type Si(111) (doped with phosphorus) with a resistivity of 1–5 kΩ cm (carrier concentration ∼10^{13} cm^{-3}) was used as a sample. The sample was placed on the motorized stage rotated relative to normal of the sample surface. The second optical harmonic generated in the specular direction with respect to the incident probe radiation was detected using a Hamamatsu R4220P photomultiplier tube (PMT) operated in the photon counting mode. The polarization of the generated SH was filtered by a Glan prism P2 placed in front of the PMT. A BG39 filter was placed in front of the Glan prism to cut off the fundamental harmonic. In addition, to cut off external radiation, another BG39 filter and a narrow-band bandpass filter (BF) for the SH were located directly in front of the PMT. Parasitic SH radiation generated in optical elements before the sample was cut off by a color filter (CF). During the experiment, special attention was paid to adjust the rotation stage with minimum SH beam wandering as well as to orientate the P1, P2, and TP to accurately align the corresponding field polarizations.

During the experiment, it was found that, in the presence of a terahertz field, the SHG occurs not only in the sample but also in air during the joint propagation of the optical and terahertz pulses (between the off-axis parabolic mirror PM3 and the sample). The magnitude of this unwanted "air" SH signal for some polarization configurations was comparable with the SH signal from the sample (for example, in the SSS case). Physically, this can be explained by the fact that, despite the significantly lower air nonlinearity compared to silicon, the interaction length of the fundamental and SHs in air, which also determines the amplitude of the SH signal [68], is several orders of magnitude longer (2 cm of coherent length in air vs $L_{\rm SH}$ ∼ 50 nm in Si). To minimize the air signal, some part of the experimental setup containing the sample was placed in a container filled with helium, which has an order of magnitude less nonlinear than air [69,70]. This reduced the air signal by ∼2 orders of magnitude. Note that some measurements were performed in ambient air due to certain experimental restrictions. In this case, the results were appropriately recalculated.

Figures 4–6 show the SH signal (a number of detected SH photos from 15 000 laser pulses) as a function of the azimuthal rotation angle (Figs. 4 and 6) and the terahertz field magnitude (Fig. 5) for different polarization configurations. The measurements demonstrate that the intense terahertz field (>100 kV/cm) significantly affects the SH signal value and its azimuthal dependences when the polarizations of the terahertz field and SH radiation coincide (the SSS, PSS, SP$_\pm$P, and PP$_\pm$P cases). For other cases (PP$_\pm$S, SP$_\pm$S, SSP, and PSP), the impact of the terahertz field is insignificant.

Let us analyze the obtained experimental data using Eqs. (7) and (8) and Table I in more detail. For the SS case [see Figs. 4(a) and 4(b)], the SH signal azimuthal dependence

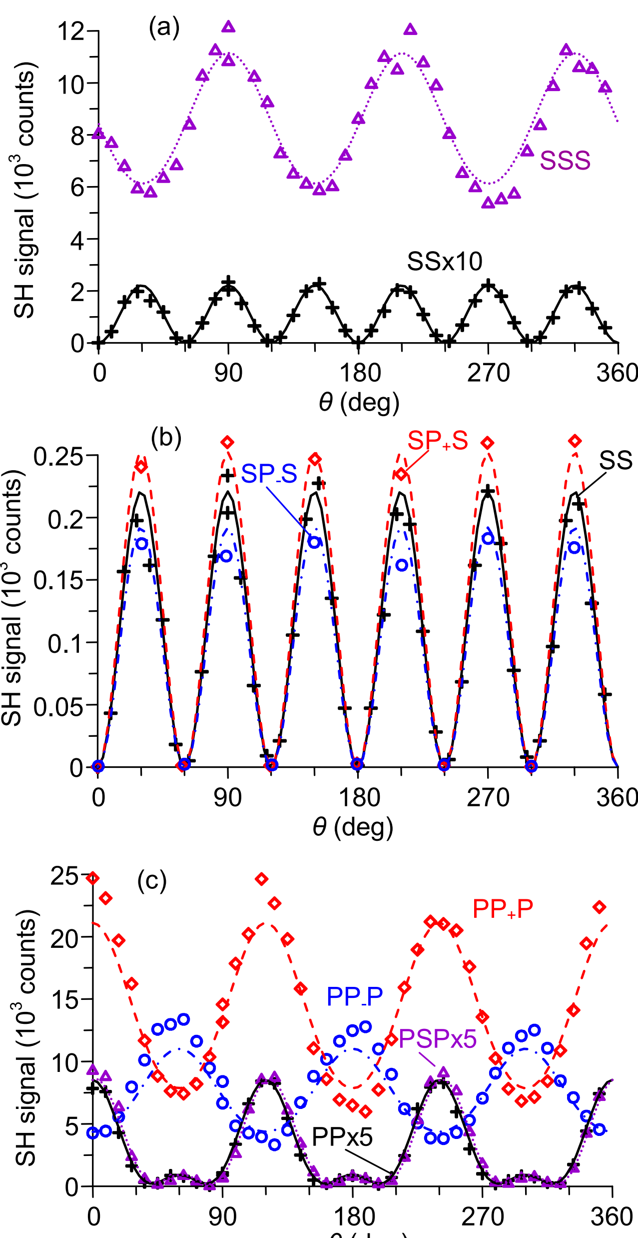

FIG. 4. Azimuthal dependences of the second-harmonic (SH) signal for (a) the SS (crosses and solid curve) and SSS (triangles and dotted curve), (b) SS, SP$_+$S (diamonds and dashed curve) and SP$_-$S (circles and dash-dotted curve), and (c) PP (crosses and solid curve), PSP (triangles and dotted curve), PP$_+$P (diamonds and dashed curve), and PP$_-$P (circles and dash-dotted curve) cases. The dots correspond to the experimental data and the curves to the theoretical calculation (see the text). Note that the SS dependence is multiplied by 10 and the PP and PSP dependences by 5. The terahertz field is E_0^T = 250 kV/cm.

is well fitted by the sixfold anisotropic function $W_{\rm SS}(\theta) = [A^{\rm a}_{\rm SS}\sin(3\theta)]^2$, in full agreement with the theory (see Table I) and the earlier studies [6,7,15,21,57]. Note that we did not observe a pedestal of the SH signal arising in the presence of microroughness of the silicon surface [12,15], which indicates a sufficiently smooth surface of our sample. When an *s*-polarized terahertz field (with E_0^T = 250 kV/cm) is imposed

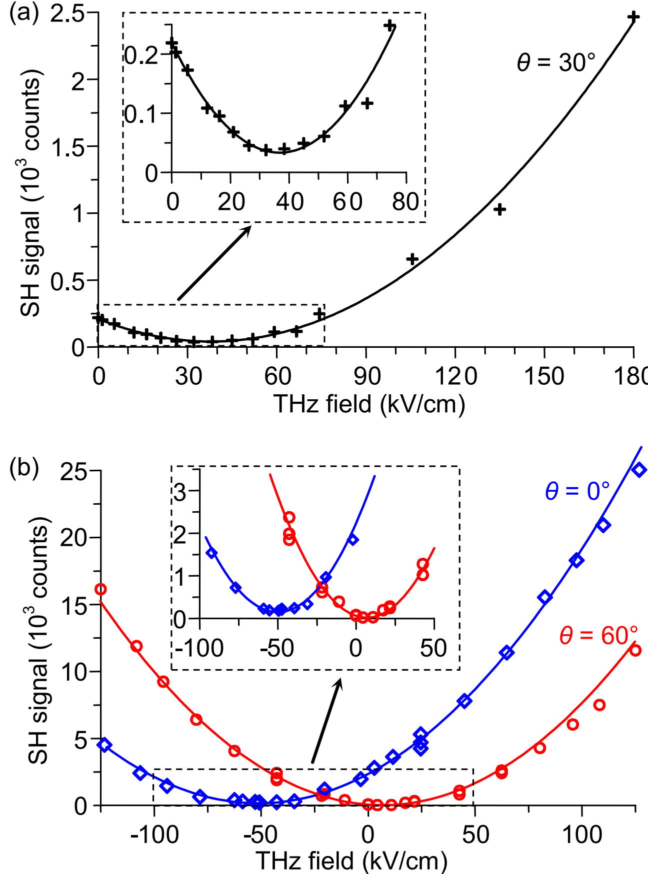

FIG. 5. Second-harmonic (SH) signal as a function of the terahertz field E_0^T for (a) the SSS and (b) PPP cases. Solid curves show the approximation of experimental data by a quadratic dependence.

on a sample, the azimuthal dependence changes significantly [Fig. 4(a)]: the sixfold anisotropy transforms to threefold anisotropy with isotropic addition, while the value of the SH signal increases drastically (by ∼50 times). This agrees well with the theory. According to Table I, the s-polarized terahertz field should add an isotropic term to the generated SH field. Then with allowance for Eq. (8), the SH signal anisotropy can be written in the form:

$$W_{\mathrm{SSS}}(\theta) = \sin^2(3\theta)\left[A_{\mathrm{SS}}^{\mathrm{a}} \sin\left(\varphi_{\mathrm{SS}}^{\mathrm{a}}\right)\right]^2 + \left[\sin(3\theta) A_{\mathrm{SS}}^{\mathrm{a}} \cos\left(\varphi_{\mathrm{SS}}^{\mathrm{a}}\right) + A_{\mathrm{SSS}} E_0^T\right]^2. \quad (9)$$

Fitting experimental data by Eq. (9) showed that $|A_{\mathrm{SS}}^{\mathrm{a}}| \ll |A_{\mathrm{SSS}} E_0^T|$ and the phase $\varphi_{\mathrm{SS}}^{\mathrm{a}}$ should not exceed 30 °. For a more accurate phase determination, we measured the SH signal as a function of the terahertz field strength at $\theta = 30^\circ$ [see Fig. 5(a)]. At this azimuthal angle, the dependence $W_{\mathrm{SSS}}(E_0^T)$, according to Eq. (9), has a minimum $W_{\mathrm{SSS}}^{\min} = [A_{\mathrm{SS}}^{\mathrm{a}} \sin(\varphi_{\mathrm{SS}}^{\mathrm{a}}]^2$ for a certain field $E_{0\min}^T$. This minimum ($W_{\mathrm{SSS}}^{\min} \approx 36$ counts) is clearly observed in Fig. 5(a) at $E_{0\min}^T = 40$ kV/cm. Then the phase $\varphi_{\mathrm{SS}}^{\mathrm{a}}$ can be found from the expression $\sin(\varphi_{\mathrm{SS}}^{\mathrm{a}}) = \pm\sqrt{W_{\mathrm{SSS}}^{\min}/W_{\mathrm{SSS}}^{0}}$, where W_{SSS}^{0} is the SH signal at $E_0^T = 0$ $[W_{\mathrm{SSS}}(E_0^T = 0) = (A_{\mathrm{SS}}^{\mathrm{a}})^2]$. From Fig. 5(a), we have $W_{\mathrm{SSS}}^{0} \approx 220$ counts, which gives $\varphi_{\mathrm{SS}}^{\mathrm{a}} \approx \pm 24^\circ$.

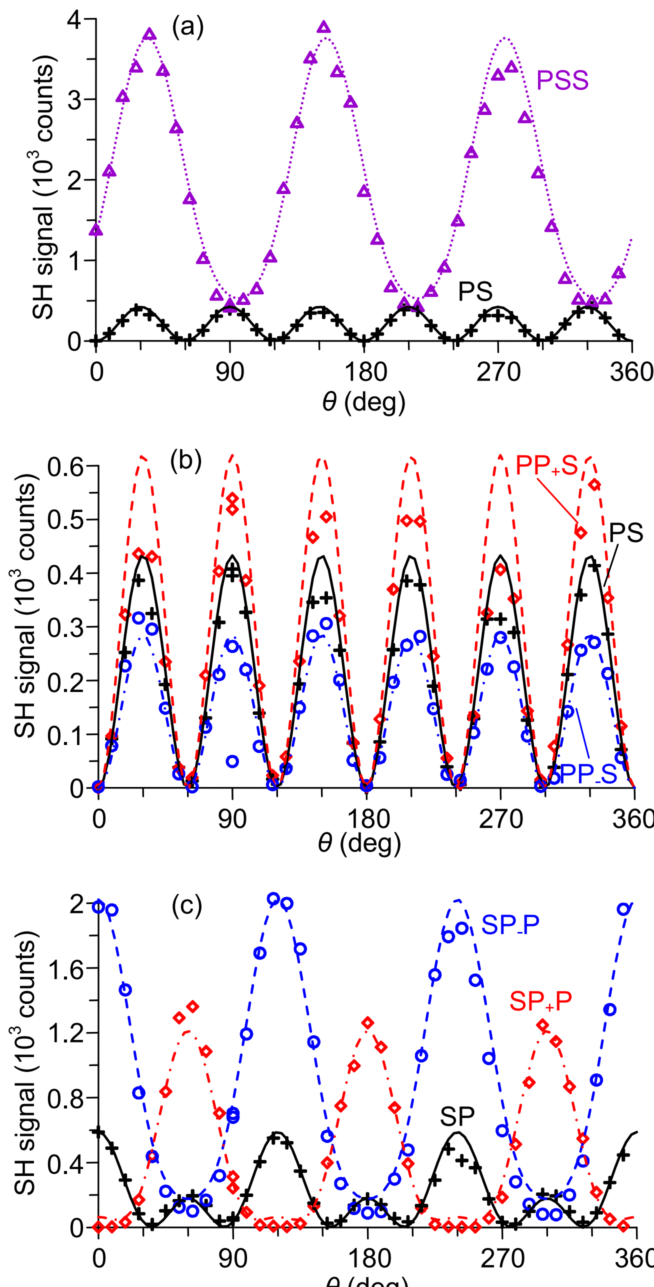

FIG. 6. Azimuthal dependences of the second-harmonic (SH) signal for (a) the PS (crosses and solid curve) and PSS (triangles and dotted curve), (b) PS and PP$_+$S (diamonds and dashed curve), and PP$_-$S (circles and dash-dotted curve), and (c) SP (crosses and solid curve), SP$_+$P (diamonds, dashed curve), and SP$_-$P (circles and dash-dotted curve) cases. The dots correspond to the experimental data and the curves to the theoretical calculation (see the text). The terahertz field $E_0^T = 250$ kV/cm.

When in the SS case a p-polarized terahertz field is applied, the form of the rotational anisotropy of the SH signal does not change [see Fig. 4(b)]. Indeed, according to Table I, the terahertz-induced SH field has the same azimuthal dependence $A_{\mathrm{SPS}} \sin(3\theta) p_T E_0^T$ (where $p_T = 1$ and $p_T = -1$ for the SP$_+$S and SP$_-$S cases, respectively) as the SH field in the SS case $A_{\mathrm{SS}}^{\mathrm{a}} \exp(i\varphi_{\mathrm{SS}}^{\mathrm{a}}) \sin(3\theta)$, which

gives $W_{SPS}(\theta) = \sin^2(3\theta)|A^a_{SS}\exp(i\varphi^a_{SS}) + A_{SPS}p_T E^T_0|^2$. However, the magnitude of the SH signal maxima increases (slightly) with the positive projection of the terahertz field on the x axis (the SP_+S case) and decreases for the opposite direction (the SP_-S case). This behavior indicates the smallness of the phase φ^a_{SS}, in accordance with the above estimated value [in the opposite case of φ^a_{SS} close to 90 °, a different terahertz field sign would give only an increase of the maxima in the $W_{SPS}(\theta)$ dependence].

Let us examine the terahertz field effect on the SHG in the PP case [Fig. 4(c)]. The SH signal rotational anisotropy in this case has six maxima of different amplitudes and is well described by the function $W_{PP}(\theta) = [A^i_{PP}\exp(i\varphi^i_{PP}) + A^a_{PP}\exp(i\varphi^a_{PP})\cos(3\theta)]^2$ [see Table I and Eq. (8)], in agreement with the previous experimental measurements [21,38,57]. When the terahertz field is turned on, the SH signal azimuthal dependence is changed similarly to the SSS case: sixfold anisotropy is converted to threefold with an isotropic addition. Switching the sign of the terahertz field (the PP_+P and PP_-P cases) changes the isotropic level and inverts the minima to maxima. According to the theory, the application of the p-polarized terahertz field should add both isotropic and anisotropic terms to the SH field. From the form of the experimental dependences, it is obvious that the magnitude of the isotropic component should be much larger than the anisotropic one (otherwise, the SH signal would have a sixfold anisotropy). Note that a significant dependence of the isotropic component on the external field normal to the surface (which is related to our PPP configuration) was also observed for DC-biased Si in the MOS structures [53,55,57] and for Si/electrolyte (Si/SiO_2/electrolyte) interfaces [71]. The application of an s-polarized terahertz field in our experiment gives only a slight variation in the SH signal anisotropy: the maximum magnitudes increase by several percent, and the azimuthal dependence shifts by several degrees along the θ axis.

To estimate the phases of the isotropic and anisotropic terms in $W_{PP}(\theta)$ of Eq. (8) (φ^i_{PP} and φ^a_{PP}, respectively), the SH signal as a function of the terahertz field strength was measured for the PPP case at the azimuthal angles $\theta = 0^\circ$ and 60° [Fig. 5(b)], which correspond to the major and minor maxima in Fig. 4(c), respectively. The analysis of the obtained terahertz field dependences in Fig. 5(b), like that carried out for the SSS case, made it possible to estimate the values of φ^i_{PP} and φ^a_{PP} in the range 15 °–20 °.

The effect of the terahertz field on the SHG with orthogonal polarizations of the fundamental and second optical harmonics (the PSS, $PP_\pm S$, and $SP_\pm P$ cases) is shown in Fig. 6. In the $SP_\pm P$ and PSS cases, where the polarizations of terahertz field and SH radiation are parallel, strong changes in the SH signal rotation anisotropy are observed relative to the SP and PS cases, respectively. These changes, like the SSS and PPP cases, indicate adding a relatively large isotropic component to the corresponding SH fields under the action of the terahertz field. Azimuthal dependences in the $PP_\pm S$ and PS cases differ only in amplitude, which exhibits the addition of a small anisotropic component when the terahertz field is turned on. All experimental dependences in Fig. 6 are consistent with Eq. (8) and the theoretical formulas from Table I for respective polarizations. The analysis shows that the phases $\varphi^{i,a}_{SP}$ and φ^a_{PS} in Eq. (8) lie in the range 15 °–25 °.

Summarizing the above-discussed experimental results, we can say that, first, the phase of the SH field $\mathbf{E}^0_{SH}$ (without the external terahertz field) and the phase of TFI SH field $\mathbf{E}^T_{SH}$ are close for any polarization configuration. Second, the main impact of the terahertz field on the rotation anisotropy of the SH signal is the addition of a significant (for $E^T_0 > 100$ kV/cm) isotropic component.

We now discuss the obtained results from the point of view of the relationship between different mechanisms of SHG. First, we should note that, in our experimental conditions, the frequencies of the fundamental and SHs are far from the silicon resonances. Indeed, for the used laser radiation at the central wavelength 790 nm and the full width at half maximum bandwidth 20 nm, the energy of the SH photons lies in the range 3.14 ± 0.06 eV. This range is fairly far from the resonances related to interband transitions in silicon (critical points near $E'_0, E_1 \approx 3.4$ eV and $E_2 \approx 4.3$–4.5 eV), even with allowance for strained Si-Si bonds in the silicon interface (leading to a shift of the E'_0, E_1 critical points to 3.3 eV) [25,28,35]. This fact allows us to consider the components of the nonlinear susceptibility tensors as real quantities [30,72] and use Eq. (7) in the further consideration.

The analysis of the measured azimuthal dependences of the SH signal using Eqs. (7) and (8) with allowance for the obtained phenomenological phases $\varphi^{i,a}_{RR} \sim 15^\circ$–$25^\circ$ (R = S, P) has led to two important conclusions. First, the amplitude of the SH field generated by the surface and the quadrupole NPs should be >2 times less than the amplitude of the EFI SH field. In Eq. (7), this corresponds to the following relation:

$$F^S_{RR} + F^Q_{RR} \approx (0.4 \pm 0.05)F^B_{RR}. \quad (9)$$

Second, the phases of the SH fields induced by the built-in and terahertz fields should be close ($\varphi^B \approx \varphi^T$) and shifted by $\pi/2$ relative to the phase of the SH fields from the surface and quadrupole sources (as a result, the SH fields $\mathbf{E}^S_{SH} + \mathbf{E}^Q_{SH}$ do not interfere with $\mathbf{E}^B_{SH} + \mathbf{E}^T_{SH}$). Note that, in accordance with Fig. 2, the obtained equality of the φ^B and φ^T phases requires a long localization length of the build-in field $L^B \gg L_{SH}$. Indeed, for a carrier concentration of $\sim 10^{13}$ cm^{-3} in our sample, the estimation gives $L^B \sim 500$ nm, which is much greater than $L_{SH} \approx 50$ nm.

Thus, we can say that the SHG from our sample is mainly determined by the EFISHG effect, where the electric field is either the built-in field alone or the superposition of the built-in and terahertz fields (in the absence of the terahertz field, the built-in field contribution to the SH signal is >80%). This allows us to determine the ratio between the $\hat{\chi}^{(3)}$ tensor components and the magnitude of the built-in field E^B. To determine the ratio between χ_1, χ_2, and χ_3, it is sufficient to use the azimuthal dependences of the measured SH signal for the SS (or PS), SP, and PP cases (without the terahertz field). We fitted these dependences by Eq. (7), where the functions F^B_{RR} (R = S, P) were obtained from the corresponding components of the SH electric field $\mathbf{E}^B$ calculated by Eq. (6) (see also Ref. [1]) with allowance for anisotropy of the built-in field-induced NP $\mathbf{P}^B$ (Table I). Minor functions $F^{S,Q}_{RR}$ were also considered in Eq. (7) with magnitudes corresponding to Eq. (9). As a result, we found $\chi_0 \approx -0.13\chi_1$ and $\chi_2 \approx \chi_3$ (with accuracy up to a few percent), which gives the following relation: $\chi_3 \approx \chi_2 \approx (0.51 \pm 0.02)\chi_1$.

The experimentally obtained equality of the nondiagonal tensor $\hat{\chi}^{(3)}(2\omega;\omega,\omega,0)$ components $\chi_3 \equiv \chi_{1221}$ and $\chi_2 \equiv \chi_{1212}$ formally corresponds to the Kleinman symmetry, although the applicability of this symmetry is not obvious due to the presence of absorption bands between the interacting (optical and terahertz) frequencies [72,73]. Note that this equality follows from the simplified bond-hyperpolarizability model [74].

It is interesting to compare the silicone anisotropy parameters $\sigma_{\rm EFISHG} = [2\chi_2^{(3)} + \chi_3^{(3)}]/\chi_1^{(3)} - 1 = 6\chi_0/(\sqrt{2}\chi_1)$ and $\sigma_{\rm THG} = 3\chi_{1212}^{(3)}(3\omega)/\chi_{1111}^{(3)}(3\omega) - 1$, where the latter is introduced for third-harmonic generation (THG) governed by the tensor $\hat{\chi}^{(3)}(3\omega;\omega,\omega,\omega)$ [7]. From previous experimental works, the measured anisotropy parameter for $\hat{\chi}^{(3)}(3\omega;\omega,\omega,\omega)$ was about $\sigma_{\rm THG} \approx 0.6$–$0.7$ at $\lambda_\omega \sim 770$ nm [19,75] and $\sigma_{\rm THG} \approx 0.7$–$0.85$ at $\lambda_\omega \sim 820$ nm [75,76]. From our data for $\hat{\chi}^{(3)}(2\omega;\omega,\omega,0)$, we have $\sigma_{\rm EFISHG} \approx 0.54 \pm 0.05$ at $\lambda_\omega = 790$ nm. As is seen, $\sigma_{\rm EFISHG}$ and $\sigma_{\rm THG}$ are close, especially if a theoretically calculated nonmonotonic dispersion of $\sigma_{\rm THG}$ in the optical range 750–850 nm is considered [75].

Let us estimate the absolute value of the silicon third-order susceptibility, which can be found from the measured SH signal, terahertz field magnitude, and parameters of the optical pulse (intensity, duration, and beam size). For this purpose, we accurately calculated generated SH energy (considering PMT quantum efficiency and transmission coefficient of optical filters placed between the sample and PMT) and then substituted this energy in the corresponding analytical expression derived from Eq. (6) for SH electric field $\mathbf{E}_{\rm SH}^T$ (see also Refs. [1,61]) with allowance for Fresnel coefficients for fundamental and terahertz fields (for calculation, we used the SSS case). As a result, we obtained $\chi_1 \approx (1.4 \pm 0.5) \times 10^{-10}$ esu $[(1.9 \pm 0.7) \times 10^{-18}\ {\rm m^2/V^2}]$. Note that in recent experiments for EFISHG in silicon waveguides pumped at $\lambda_\omega \sim 2.3\,\mu$m, the silicon third-order susceptibility $\chi_{xxxx}^{(3)}$ was estimated in the range of 10^{-19}–$10^{-18}\ {\rm m^2/V^2}$ [77]. Since we follow the notation of Ref. [1], $\chi_1 = 3\chi_{xxxx}^{(3)}$ (cf. Refs. [72,73]), and, as can be seen, χ_1 is in a good agreement with the published data. To verify the correctness of our evaluation method, we also measured third-order susceptibility for fused quartz $\chi_{\rm SiO2}^{(3)}(2\omega;\omega,\omega,0)$ under a similar experimental condition but in transmission geometry when a plate of fused quartz (with a thickness of 3 mm) was illuminated normally by optical and terahertz pulses, and generated SH energy was measured behind the sample (see Ref. [68]). Based on equations for the SH field given in Ref. [68], we obtained $\chi_{\rm SiO2}^{(3)} \approx (2 \pm 0.6)\times 10^{-14}$ esu $[(2.8 \pm 1)\times 10^{-22}\ {\rm m^2/V^2}]$, which agrees well with early measured values $(2.3$–$3.5)\times 10^{-14}$ esu for glasses by EFISHG [78,79] and $\chi_{xxxx}^{(3)}(3\omega) \sim 1.5\times 10^{-14}$ esu for fused silica by THG [80] (see also review of the nonlinear refractive-index coefficient of fused silica in Ref. [81]).

We also studied the SH signal from the silicon surface for different time delay between optical and terahertz pulses in the SSS case at $\theta = 0$. The obtained time-delay dependence approximately traced the squared waveform of the terahertz field. This is consistent with Eq. (9) and reflects negligible dispersion of third-order susceptibility in the terahertz frequency range that is expected due to small terahertz dispersion of linear susceptibility [82].

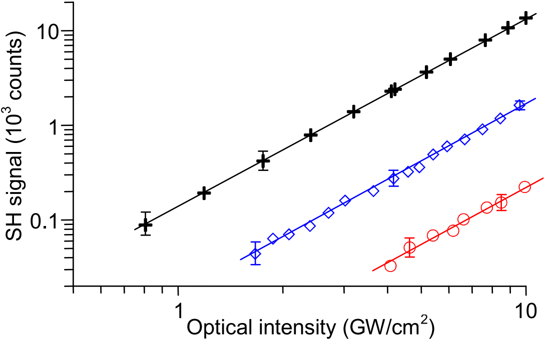

FIG. 7. Second-harmonic (SH) signal as a function of the intensity of the fundamental optical pulse for the cases PP at $\theta = 0^\circ$ (blue diamonds), SS at $\theta = 90^\circ$ (red circles), and SSS at $\theta = 90^\circ$ (black crosses). Solid straight lines correspond to the approximation of experimental data by a quadratic dependence.

To determine the built-in field, we used the measured dependence of the SH signal on the terahertz field strength for the SSS case $W_{\rm SSS}(E_0^T)$ at $\theta = 30^\circ$ [Fig. 5(a)]. At the minimum of $W_{\rm SSS}(E_0^T)$ for $E_0^T = E_{0\,\rm min}^T = 40$ kV/cm, the SH fields induced by the built-in and terahertz fields compensate for each other (the residual SH signal is generated by the surface and quadrupole sources). In this case, following Table I, we get

$$E^B = \frac{\chi_1 - \left(\frac{3}{\sqrt{2}}\right)\chi_0}{\chi_0} E_{\rm min}^T = -9.8 E_{\rm min}^T, \tag{10}$$

where $E_{\rm min}^T = T_{\rm Si} E_{0\,\rm min}^T$ is the terahertz field in silicon, and $T_{\rm Si}$ is the Fresnel transmission coefficient. For the s-polarized terahertz radiation incident at an angle of 45°, we have $T_{\rm Si} = 0.33$, which in view of Eq. (10) yields $E^B = -130$ kV/cm. The negative sign of E^B indicates that the built-in field is directed against the z axis, namely, from the Si bulk to the surface. This is consistent with the negative sign of the charged Si-SiO_2 interface governed by the n-type doping of the sample. Estimation of the surface charge density gives $\sim 10^{12}\ {\rm cm^{-2}}$, which is consistent with the possible density of the electron-trapped surface states in the Si-SiO_2 interface [34,43].

The strength of the built-in field is determined by the properties of the particular silicon sample (carrier concentration, surface quality, oxide thickness, etc.), but it can also be changed under light irradiation [42–47,54,83]. It was mentioned in the Introduction that, when the silicon surface is exposed to laser radiation, photoinduced carriers can be trapped in the Si interface or in the SiO_2 layer, which can lead to a variation in the built-in field and, consequently, change the SH signal. In our experiment, we checked the possible presence of this effect by measuring the SH signal as a function of the intensity (energy) of the fundamental laser pulse for the SS and PP cases (see Fig. 7). The measurement results did not reveal any deviation of the SH signal from the quadratic dependence up to the maximum optical intensity $10\ {\rm GW/cm^2}$ within experimental accuracy, which indicates that the electron trapping effect is negligible. This is consistent with the TD-SHG measurement, where the effect was also

TABLE II. Fitted F^B_{RR} and calculated F^T_{RRR} functions (see text).

Fitted function	Calculated function	
$F^B_{\mathrm{SS}} = -0.43\sin(3\theta)$	$F^T_{\mathrm{SSS}} = 2.9$	$F^T_{\mathrm{SPS}} = -p_T 0.035\sin(3\theta)$
$F^B_{\mathrm{PS}} = 0.6\sin(3\theta)$	$F^T_{\mathrm{PSS}} = 1.3{-}0.16\cos(3\theta)$	$F^T_{\mathrm{PPS}} = p_T 0.14\sin(3\theta)$
$F^B_{\mathrm{SP}} = 0.54\cos(3\theta) + 0.18$	$F^T_{\mathrm{SSP}} = -0.045\sin(3\theta)$	$F^T_{\mathrm{SPP}} = p_T(-0.7 + 0.02\cos(3\theta))$
$F^B_{\mathrm{PP}} = -0.5\cos(3\theta) - 0.76$	$F^T_{\mathrm{PSP}} = -0.14\sin(3\theta)$	$F^T_{\mathrm{PPP}} = p_T(-3{-}0.14\cos(3\theta))$

weakly pronounced at the same intensity level, even for a much higher laser repetition rate (∼100 MHz) [47].

Photogenerated carriers in silicon can also lead to screening of both the built-in [54] and terahertz fields. The estimation of the induced electron density (localized at a penetration length of ∼10 μm for the fundamental harmonic) at the maximum optical intensity (∼10 GW/cm^2) gives a value of ∼ 2×10^{18} cm^{-3}. The characteristic screening time of the electric field in this case can be estimated as $\sim 1/\omega_p$ (ω_p is the plasma frequency of photogenerated carriers) [54] and is several tens of femtoseconds, which is comparable with the optical pulse duration ∼70 fs. With such estimates, one can expect the effect of the carrier excitation on the SHG. However, like the SS and PP cases, the measurements of the SSS and PPP signals vs fundamental harmonic intensity (only the SSS case is given in Fig. 7) did not show any deviation from the quadratic dependence. It is quite possible that the actual screening time is increased due to collisions of hot photogenerated carriers, comparable with the plasma frequency [84]. In addition, the plasma formation is an integral process and occurs with some delay relative to the peak of the optical pulse, when the SH is most efficiently generated.

With found relation between the $\hat{\chi}^{(3)}$ tensor components and the magnitude of the built-in field, the terahertz-induced amplitude terms F^T_{RRR} in Eq. (7) were calculated considering Table I (without any additional adjustment factors) and shown in the central and right columns of Table II. The fitted functions F^B_{RR} are shown in the left column of Table II. The resulting azimuthal dependences of the SH signal are depicted in Figs. 4 and 5. Good agreement between the theoretical calculation and the experimental data is observed, which indicates the correctness of the obtained relation between $\hat{\chi}^{(3)}$ components and magnitude of built-in electric field E^B.

It can be seen in Table II that, for the SSS, PSS, SPP, and PPP cases, the presence of the terahertz field adds for the SH field mainly an isotropic component. This is because, as was mentioned in Sec. II, the anisotropic term of the TFI SH field has an amplitude coefficient proportional to the anisotropy constant χ_0 (see Table I), which is several times smaller than the tensor components χ_1, χ_2, and χ_3. For the same reason, the effect of the terahertz field on the SHG is insignificant for the SPS, SSP, PPS, and PSP cases, where only the anisotropic term is added. For the SPS case, the TFI term of the SH field has an amplitude of only ∼8% relative to the SH field amplitude for the SS case (see F^T_{SPS} and F^B_{SS} in Table II). Nevertheless, such a slight change was observed in the experiment [see Fig. 4(b)]. In the PPS case, the effect of the terahertz field on the PS azimuthal dependence is 3–4 times stronger (see a comparison of F^B_{SS} with F^T_{SPS} and of F^B_{PS} with F^T_{PPS} in Table II), which should give a ∼40–50% change in the PS signal amplitude. In the experiment, a slightly smaller change (by ∼30%) was observed; nevertheless, the result qualitatively agrees with the theory [Fig. 6(b)]. In the PSP case, the terahertz field adds a small (with a threefold less amplitude) anisotropic component in quadrature with respect to the anisotropic component of the SH field in the PP case (F^B_{PP} and F^T_{PSP} in Table II). This should lead to a shift of the PSP signal azimuthal dependence along the θ axis by several degrees and an insignificant (by several percent) increase in the signal, which also agrees with the experimental results [Fig. 4(c)].

IV. CONCLUSIONS

To conclude, comprehensive experimental and theoretical studies of the second optical harmonic generation from the surface of low-doped Si(111) with native oxide under irradiation with femtosecond optical and picosecond terahertz pulses (with a terahertz peak field of up to 250 kV/cm) were performed. From the phenomenological approach, the theory of the EFISHG azimuthal rotation anisotropy for Si(111) was extended by considering the arbitrary polarization of the external (terahertz) electric field. The theory showed that, for the some polarization configuration, a terahertz field can modify the angular anisotropy of the SH energy (signal). It was found from the experiment that this modification occurs when the polarizations of the terahertz and SH fields coincide and consist of adding an isotropic term in the corresponding azimuthal dependences. Analysis of the SH signal as a function of the azimuthal angle and the terahertz field strength for different polarization configurations allows us to judge the dominant mechanism of SHG. For the sample under study, it was established that the main source of SH (without the terahertz external influence) is the built-in field-induced NP, and the contribution to the SH signal from the surface and quadrupole nonlinear sources does not exceed 20%. This fact makes it possible to find the magnitude of the built-in electric field (∼130 kV/cm), estimate the silicon third-order susceptibility $\chi_1 = 3\chi^{(3)}_{xxxx} \approx (1.4 \pm 0.5)\times 10^{-10}$ esu [$(1.9 \pm 0.7)\times 10^{-18}$ m^2/V^2], and determine the ratio between the tensor $\hat{\chi}^{(3)}(2\omega;\omega,\omega,0)$ components, the ratio being characterized by the EFISHG anisotropy parameter $\sigma_{\mathrm{EFISHG}} = [2\chi^{(3)}_{1212} + \chi^{(3)}_{1221}]/\chi^{(3)}_{1111} - 1 \approx 0.54 \pm 0.05$ at 790 nm fundamental wavelength.

ACKNOWLEDGMENT

This paper was supported by the Ministry of Science and Higher Education of the Russian Federation (No. 0729-2020-0035) and by the Russian Foundation for Basic Research (No. 18-29-19091mk).

[1] O. A. Aktsipetrov, I. M. Baranova, and K. N. Evtyukhov, *Second Order Non-linear Optics of Silicon and Silicon Nanostructures*, 1st ed. (CRC Press, Boca Raton, 2016).

[2] M. Cazzanelli and J. Schilling, Second order optical nonlinearity in silicon by symmetry breaking, Appl. Phys. Rev. **3**, 011104 (2016).

[3] M. C. Downer, B. S. Mendoza, and V. I. Gavrilenko, Optical second harmonic spectroscopy of semiconductor surfaces: Advances in microscopic understanding, Surf. Interface Anal. **31**, 966 (2001).

[4] G. Lupke, Characterization of semiconductor interfaces by second-harmonic generation, Surf. Sci. Rep. **35**, 75 (1999).

[5] T. F. Heinz, Chapter 5—Second-order nonlinear optical effects at surfaces and interfaces, Mod. Probl. Condens. Matter Sci. **29**, 353 (1991).

[6] H. W. K. Tom, T. F. Heinz, and Y. R. Shen, Second-Harmonic Reflection from Silicon Surfaces and Its Relation to Structural Symmetry, Phys. Rev. Lett. **51**, 1983 (1983).

[7] J. E. Sipe, D. J. Moss, and H. M. van Driel, Phenomenological theory of optical second- and third-harmonic generation from cubic centrosymmetric crystals, Phys. Rev. B **35**, 1129 (1987).

[8] T. F. Heinz, M. M. T. Loy, and W. A. Thompson, Study of symmetry and disordering of Si(111)-7×7 surfaces by optical second harmonic generation, J. Vac. Sci. Technol. B **3**, 1467 (1985).

[9] T. F. Heinz, M. M. T. Loy, and W. A. Thompson, Study of Si(111) Surfaces by Optical Second-Harmonic Generation: Reconstruction and Surface Phase Transformation, Phys. Rev. Lett. **54**, 63 (1985).

[10] L. L. Kulyuk, D. A. Shutov, E. E. Strumban, and O. A. Aktsipetrov, Second-harmonic generation by an SiO_2-Si interface: influence of the oxide layer, J. Opt. Soc. Am. B **8**, 1766 (1991).

[11] J. Y. Huang, Probing inhomogeneous lattice deformation at interface of Si(111)/SiO_2 by optical second-harmonic reflection and Raman spectroscopy, Jpn. J. Appl. Phys. **33**, 3878 (1994).

[12] J. I. Dadap, B. Doris, Q. Deng, M. C. Downer, J. K. Lowell, and A. C. Diebold, Randomly oriented Angstrom-scale microroughness at the Si(100)/SiO_2 interface probed by optical second harmonic generation, Appl. Phys. Lett. **64**, 2139 (1994).

[13] Y. Q. An and S. T. Cundiff, Bulk and surface contributions to resonant second-harmonic generation from Si(001) surfaces, Appl. Phys. Lett. **81**, 5174 (2002).

[14] D. Bodlaki and E. Borguet, *In situ* second-harmonic generation measurements of the stability of Si(111)-H and kinetics of oxide regrowth in ambient, J. Appl. Phys. **95**, 4675 (2004).

[15] O. A. Aktsipetrov, I. M. Baranova, and Yu. A. Il'inskii, Contribution of the surface in the generation of reflected second harmonic for centrosymmetric semiconductors, Sov. Phys. JETP **64**, 167 (1986).

[16] R. Ehlert, J. Kwon, L. Loumakos, O. Sharia, A. A. Demkov, and M. C. Downer, Optical second-harmonic and reflectance-anisotropy spectroscopy of clean and hydrogen-terminated vicinal Si(001) surfaces, J. Opt. Soc. Am. B **27**, 981 (2010).

[17] J. F. McGilp, Using steps at the Si-SiO_2 interface to test simple bond models of the optical second-harmonic response, J. Phys.: Condens. Matter **19**, 016006 (2007).

[18] G. Lüpke, D. J. Bottomley, and H. M. van Driel, SiO_2/Si interfacial structure on vicinal Si(100) studied with second-harmonic generation, Phys. Rev. B. **47**, 10389 (1993).

[19] G. Lüpke, D. J. Bottomley, and H. M. van Driel, Second- and third-harmonic generation from cubic centrosymmetric crystals with vicinal faces: phenomenological theory and experimenl [sic], J. Opt. Soc. Am. B **11**, 33 (1994).

[20] C. Meyer, G. Lüpke, U. Emmerichs, F. Wolter, H. Kurz, C. H. Bjorkman, and G. Lucovsky, Electronic Transition at Si(111)/SiO_2 and Si(111)/Si_3N_4 Interfaces Studied by Optical Second-Harmonic Spectroscopy, Phys. Rev. Lett. **74**, 3001 (1995).

[21] S. V. Govorkov, V. I. Emel'yanov, N. I. Koroteev, G. I. Petrov, I. L. Shumay, and V. V. Yakovlev, Inhomogeneous deformation of silicon surface layers probed by second-harmonic generation in reflection, J. Opt. Soc. Am. B **6**, 1117 (1989).

[22] J. H. Zhao, W. Su, Q. D. Chen, Y. Jiang, Z. G. Chen, G. Jia, and H. B. Sun, Strain at native SiO_2/Si(111) interface characterized by strain-scanning second-harmonic generation, IEEE J. Quantum Electron. **47**, 55 (2011).

[23] T. F. Heinz, F. J. Himpsel, E. Palange, and E. Burstein, Electronic Transitions at the CaF_2/Si(111) Interface Probed by Resonant Three-Wave Mixing Spectroscopy, Phys. Rev. Lett. **63**, 644 (1989).

[24] W. Daum, H.-J. Krause, U. Reichel, and H. Ibach, Nonlinear optical spectroscopy at silicon interfaces, Phys. Scr. **T49**, 513 (1993).

[25] G. Erley and W. Daum, Silicon interband transitions observed at Si(100)-SiO_2 interfaces, Phys. Rev. B **58**, R1734 (1998).

[26] S. Bergfeld, B. Braunschweig, and W. Daum, Nonlinear Optical Spectroscopy of Suboxides at Oxidized Si(111) Interfaces, Phys. Rev. Lett. **93**, 097402 (2004).

[27] P. T. Wilson, Y. Jiang, O. A. Aktsipetrov, E. D. Mishina, and M. C. Downer, Frequency-domain interferometric second-harmonic spectroscopy, Opt. Lett. **24**, 496 (1999).

[28] W. Daum, Optical studies of Si/SiO_2 interfaces by second-harmonic generation spectroscopy of silicon interband transitions, Appl. Phys. A **87**, 451 (2007).

[29] V. I. Gavrilenko, Differential reflectance and second-harmonic generation of the Si/SiO_2 interface from first principles, Phys. Rev. B **77**, 155311 (2008).

[30] T. V. Dolgova, A. A. Fedyanin, and O. A. Aktsipetrov, dc-electric-field-induced second-harmonic interferometry of the Si(111)-SiO_2 interface in Cr-SiO_2-Si MOS capacitor, Phys. Rev. B **68**, 073307 (2003).

[31] N. M. Terlinden, V. Vandalon, R. H. E. C. Bosch, and M. M W. (Erwin) Kessels, Second-harmonic intensity and phase spectroscopy as a sensitive method to probe the space-charge field in Si(100) covered with charged dielectrics, J. Vac. Sci. Technol. A **32**, 021103 (2014).

[32] R. W. Terhune, P. D. Maker, and C. M. Savage, Optical Harmonic Generation in Calcite, Phys. Rev. Lett. **8**, 404 (1962).

[33] V. M. Arutyunyan, Physical properties of the semiconductor-electrolyte interface, Sov. Phys. Usp. **32**, 521 (1989).

[34] S. M. Sze and K. K. Ng, *Physics of Semiconductor Devices*, 3rd ed. (John Wiley & Sons, New Jersey, 2007).

[35] W. Daum, H.-J. Krause, U. Reichel, and H. Ibach, Identification of Strained Silicon Layers at Si-SiO_2 Interfaces and Clean Si Surfaces by Non-Linear Optical Spectroscopy, Phys. Rev. Lett. **71**, 1234 (1993).

[36] H. J. Peng, E. J. Adles, J.-F. T. Wang, and D. E. Aspnes, Relative bulk and interface contributions to optical second-harmonic generation in silicon, Phys. Rev. B **72**, 205203 (2005).

[37] O. A. Aktsipetrov, A. A. Fedyanin, A. V. Melnikov, J. I. Dadap, X. F. Hu, M. N. Anderson, M. C. Downer, and J. K. Lowell, D.c. electric field induced second-harmonic generation spectroscopy of the Si(001)-SiO_2 interface: separation of the bulk and surface non-linear contributions, Thin Solid Films **294**, 231 (1997).

[38] C. Reitböck, D. Stifter, A. Alejo-Molina, K. Hingerl, and H. Hardhienata, Bulk quadrupole and interface dipole contribution for second harmonic generation in Si, J. Opt. **18**, 035501 (2016).

[39] E. H. Nicollian and J. R. Brews, *MOS (Metal Oxide Semiconductor) Physics and Technology* (John Wiley & Sons, Somerset, 1982).

[40] D. K. Schroder, *Semiconductor Material and Device Characterization*, 3rd ed. (John Wiley & Sons, Hoboken, 2006).

[41] F. Palumbo, C. Wen, S. Lombardo, S. Pazos, F. Aguirre, M. Eizenberg, F. Hui, and M. Lanza, A review on dielectric breakdown in thin dielectrics: Silicon dioxide, high-k, and layered dielectrics, Adv. Funct. Mater. **30**, 1900657 (2020).

[42] M. L. Alles, R. Pasternak, X. Lu, N. H. Tolk, R. D. Schrimpf, D. M. Fleetwood, R. P. Dolan, and R. W. Standley, Second harmonic generation for noninvasive metrology of silicon-on-insulator wafers, IEEE Trans. Semicond. Manuf. **20**, 107 (2007).

[43] J. G. Mihaychuk, J. Bloch, Y. Liu, and H. M. Van Driel, Time-dependent second-harmonic generation from the Si-SiO_2 interface induced by charge transfer, Opt. Lett. **20**, 2063 (1995).

[44] J. Bloch, J. Mihaychuk, and H. van Driel, Electron Photoinjection from Silicon to Ultrathin SiO_2 Films via Ambient Oxygen, Phys. Rev. Lett. **77**, 920 (1996).

[45] J. L. Fiore, V. V. Fomenko, D. Bodlaki, and E. Borguet, Second harmonic generation probing of dopant type and density at the Si/SiO_2 interface, Appl. Phys. Lett. **98**, 041905 (2011).

[46] B. Jun, Y. V. White, R. Schrimpf, D. Fleetwood, F. Brunier, N. Bresson, S. Cristoloveanu, and N. Tolk, Characterization of multiple Si/SiO_2 interfaces in silicon-on-insulator materials via second-harmonic generation, Appl. Phys. Lett. **85**, 3095 (2004).

[47] T. Scheidt, E. G. Rohwer, P. Neethling, H. M. von Bergmann, and H. Stafast, Ionization and shielding of interface states in native p^+-Si/SiO_2 probed by electric field induced second harmonic generation, J. Appl. Phys. **104**, 083712 (2008).

[48] C. Ohlhoff, G. Lupke, C. Meyer, and H. Kurz, Static and high-frequency electric fields in silicon MOS and MS structures probed by optical second-harmonic generation, Phys. Rev. B **55**, 4596 (1997).

[49] O. A. Aktsipetrov, A. A. Fedyanin, A. V. Melnikov, E. D. Mishina, A. N. Rubtsov, M. H. Anderson, P. T. Wilson, M. ter Beek, X. F. Hu, J. I. Dadap, and M. C. Downer, dc-electric-field-induced and low-frequency electromodulation second-harmonic generation spectroscopy of Si(001)-SiO_2 interfaces, Phys. Rev. B **60**, 8924 (1999).

[50] C. H. Lee, R. K. Chang, and N. Bloembergen, Nonlinear Electroreflectance in Silicon and Silver, Phys. Rev. Lett. **18**, 167 (1967).

[51] O. A. Aktsipetrov, A. A. Fedyanin, V. N. Golovkina, and T. V. Murzina, Optical second-harmonic generation induced by a dc electric field at the Si-SiO_2 interface, Opt. Lett. **19**, 1450 (1994).

[52] O. A. Aktsipetrov, A. A. Fedyanin, E. D. Mishina, A. N. Rubtsov, C. W. van Hasselt, M. A. C. Devillers, and Th. Rasing, dc-electric-field-induced second-harmonic generation in Si(111)-SiO_2-Cr metal-oxide-semiconductor structures, Phys. Rev. B **54**, 1825 (1996).

[53] O. A. Aktsipetrov, A. A. Fedyanin, J. I. Dadap, and M. C. Downer, Dc-electric-field-induced second-harmonic generation studies of surfaces and buried interfaces of column IV semiconductors, Laser Phys. **6**, 1142 (1996).

[54] J. I. Dadap, P. T. Wilson, M. H. Anderson, M. C. Downer, and M. ter Beek, Femtosecond carrier-induced screening of dc electric-field-induced second-harmonic generation at the Si(001)-SiO_2 interface, Opt. Lett. **22**, 901 (1997).

[55] J. I. Dadap, X. F. Hu, M. H. Anderson, M. C. Downer, J. K. Lowell, and O. A. Aktsipetrov, Optical second-harmonic electroreflectance spectroscopy of a Si(001) metal-oxide-semiconductor structure, Phys. Rev. B **53**, R7607 (1996).

[56] P. Godefroy, W. de Jong, C. W. van Hasselt, M. A. C. Devillers, and Th. Rasing, Electric field induced second harmonic generation spectroscopy on a metal-oxide-silicon structure, Appl. Phys. Lett. **68**, 1981 (1996).

[57] R. W. Kempf, P. T.Wilson, J. D. Canterbury, E. D. Mishina, O. A. Aktsipetrov, and M. C. Downer, Third and fourth harmonic generation at Si-SiO_2 interfaces and in Si-SiO_2-Cr MOS structures, Appl. Phys. B **68**, 325 (1999).

[58] H. Bian, Y. Guo, and H. Wang, Non-parabolic potential dependence of optical second harmonic generation from the Si(111) electrode/electrolyte interface, Phys. Chem. Chem. Phys. **20**, 29539 (2018).

[59] S. B. Bodrov, A. I. Korytin, Yu. A. Sergeev, and A. N. Stepanov, Second-harmonic generation in zinc blende crystals under combined action of femtosecond optical and strong terahertz fields, Quantum Electron. **50**, 496 (2020).

[60] A. Savel'ev, O. Chefonov, A. Ovchinnikov, A. Rubtsov, A. Shkurinov, Y. Zhu, M. Agranat, and V. Fortov, Transient optical non-linearity in p-Si induced by a few cycle extreme THz field, Opt. Express **29**, 5730 (2021).

[61] I. M. Baranova and K. N. Evtyukhov, Generation of the second harmonic and nonlinear electroreflection from the surface of a centrosymmetric semiconductor, Quantum Electron. **25**, 1198 (1995).

[62] D. Muller, T. Sorsch, S. Moccio, F. H. Baumann, K. Evans-Lutterodt, and G. Timp, The electronic structure at the atomic scale of ultrathin gate oxides, Nature (London) **399**, 758 (1999).

[63] J. E. Sipe, New Green-function formalism for surface optics, J. Opt. Soc. Am. B **4**, 481 (1987).

[64] P. Guyot-Sionnest, W. Chen, and Y. R. Shen, General considerations on optical second-harmonic generation from surfaces and interfaces, Phys. Rev. B **33**, 8254 (1986).

[65] D. Lim, M. C. Downer, and J. G. Ekerdt, Second-harmonic spectroscopy of bulk boron-doped Si(001), Appl. Phys. Lett. **77**, 181 (2000).

[66] J. A. Fülöp, L. Pálfalvi, G. Almási, and J. Hebling, Design of high energy terahertz sources based on optical rectification, Opt. Express **18**, 12311 (2010).

[67] H. Hirori, A. Doi, F. Blanchard, and K. Tanaka, Single-cycle terahertz pulses with amplitudes exceeding 1 MV/cm generated by optical rectification in $LiNbO_3$, Appl. Phys. Lett. **98**, 091106 (2011).

[68] S. B. Bodrov, Yu. A. Sergeev, A. I. Korytin, E. A. Burova, and A. N. Stepanov, Terahertz pulse induced femtosecond optical second harmonic generation in transparent media with cubic nonlinearity, J. Opt. Soc. Am. B **37**, 789 (2020).

[69] D. P. Shelton, Nonlinear-optical susceptibilities of gases measured at 1064 and 1319 nm, Phys. Rev. A. **42**, 2578 (1990).

[70] J. F. Ward and G. H. C. New, Optical third harmonic generation in gases by a focused laser beam, Phys. Rev. **185**, 57 (1969).

[71] P. R. Fischer, J. L. Daschbach, D. E. Gragson, and G. L. Richmond, Sensitivity of second harmonic generation to space charge effects at Si(111)/electrolyte and Si(111)/SiO_2/electrolyte interfaces, J. Vac. Sci. Technol. A **12**, 2617 (1994).

[72] R. W. Boyd, *Nonlinear Optics*, 2nd ed. (Academic Press, San Diego, 2003).

[73] R. L. Sutherland, D. G. McLean, and S. Kirkpatrick, *Handbook of Nonlinear Optics*, 2nd ed. (Marcel Dekker, New York, 2003).

[74] A. Alejo-Molina, K. Hingerl, and H. Hardhienata, Model of third harmonic generation and electric field induced optical second harmonic using simplified bond-hyperpolarizability model, J. Opt. Soc. Am. B **32**, 562 (2015).

[75] D. J. Moss, H. M. van Driel, and J. E. Sipe, Dispersion in the anisotropy of optical third-harmonic generation in silicon, Opt. Lett. **14**, 57 (1989).

[76] P. N. Saeta and N. A. Miller, Distinguishing surface and bulk contributions to third-harmonic generation in silicon, Appl. Phys. Lett. **79**, 2704 (2001).

[77] R. Franchi, C. Castellan, M. Ghulinyan, and L. Pavesi, Second-harmonic generation in periodically poled silicon waveguides with lateral p-i-n junctions, Opt. Lett. **45**, 3188 (2020).

[78] C. G. Bethea, Electric field induced second harmonic generation in glass, Appl. Opt. **14**, 2435 (1975).

[79] J. L. Oudar, Optical nonlinearities of conjugated molecules. Stilbene derivatives and highly polar aromatic compounds, J. Chem. Phys. **67**, 446 (1977).

[80] U. Gubler and C. Bosshard, Optical third-harmonic generation of fused silica in gas atmosphere: absolute value of the third-order nonlinear optical susceptibility $\chi^{(3)}$, Phys. Rev. B **61**, 10702 (2000).

[81] D. Milam, Review and assessment of measured values of the nonlinear refractive-index coefficient of fused silica, Appl. Opt. **37**, 546 (1998).

[82] J. Dai, J. Zhang, W. Zhang, and D. Grischkowsky, Terahertz time-domain spectroscopy characterization of the far-infrared absorption and index of refraction of high-resistivity, float-zone silicon, J. Opt. Soc. Am. B **21**, 1379 (2004).

[83] D. Damianos, G. Vitrant, A. Kaminski-Cachopo, D. Blanc-Pelissier, G. Ghibaudo, M. Lei, J. Changala, A. Bouchard, X. Mescot, M. Gri, S. Cristoloveanu, and I. Ionica, Field-effect passivation of Si by ALD-Al_2O_3: Second harmonic generation monitoring and simulation, J. Appl. Phys. **124**, 125309 (2018).

[84] M. V. Fischetti, Monte Carlo simulation of transport in technologically significant semiconductors of the diamond and zinc-blende structures. I. Homogeneous transport, IEEE Trans. Electron Devices **38**, 634 (1991).